CONDENSED MATTER PHYSICS

Voltage controlled on-demand magnonic nanochannels

Samiran Choudhury[1], Avinash Kumar Chaurasiya[1], Amrit Kumar Mondal[1], Bivas Rana[2], Katsuya Miura[3], Hiromasa Takahashi[3], YoshiChika Otani[2,4], Anjan Barman[1]*

Development of energy-efficient on-demand magnonic nanochannels (MNCs) can revolutionize on-chip data communication and processing. We have developed a dynamic MNC array by periodically tailoring perpendicular magnetic anisotropy using the electric field. Brillouin light scattering spectroscopy is used to probe the spin wave (SW) dispersion of MNCs formed by applying a static electric field at the CoFeB/MgO interface through the one-dimensional stripe-like array of indium tin oxide electrodes placed on top of Ta/CoFeB/MgO/Al_2O_3 heterostructures. Magnonic bands, consisting of two SW frequency modes, appear with a bandgap under the application of moderate gate voltage, which can be switched off by withdrawing the voltage. The experimental results are reproduced by plane wave method–based numerical calculations, and simulated SW mode profiles show propagating SWs through nanochannels with different magnetic properties. The anticrossing between these two modes gives rise to the observed magnonic bandgap.

INTRODUCTION

The massive upsurge in the communication technology has led to ever-growing device miniaturization and operational speed and pushed the modern charge-based electronic devices toward its fundamental limit because of the inherent energy waste due to ohmic loss. A ceaseless quest over the last few decades has guided toward possible alternatives in the form of chargeless information carrier by using the spin angular momentum. The spin degree of freedom can be maneuvered in the form of spin current (*1*) or spin waves (SWs: collective precessional motion of electron spins), which can be incorporated into the next-generation energy-efficient spin-based devices. SWs can have several orders of magnitude shorter wavelength than the electromagnetic waves at the same frequency, making them a potential candidate for on-chip signal processing and communication devices with dimensions down to nanometer regime and frequency up to terahertz regime. Propagation of SWs through a periodic composite magnetic medium, the so-called magnonic crystal (MC), gives rise to magnonic mini bands and reconfigurable bandgaps (BGs) (*2*). In addition, due to their intrinsic anisotropic nature, the dipolar SWs and Dzyaloshinskii-Moriya (DM) exchange SWs show directional propagation. The above properties led toward the development of many passive and active nanoscale microwave components. Consequently, the computing technology on the basis of SWs has been initiated, while a new field named magnonics (*3*) was born. Furthermore, magnon (i.e., quanta of SW) currents have much lower dissipation than ohmic loss of charge current, and interconversion between magnon current and electron-based spin and charge current has led to the emergence of a contemporary research field, known as magnon-spintronics (*4*).

Emerging as the building blocks of magnonics, MC can be treated as the magnetic analog of photonic or phononic crystal. Numerous theoretical and experimental investigations have been conducted on these MCs made of periodic distribution of magnetic elements with diverse material and geometric parameters, e.g., saturation magnetization, exchange stiffness constant, magnetic anisotropy, size, shape, lattice constant, lattice symmetry, as well as other external controllers like magnetic field, mechanical force (stress), or charge current, to provoke the modulation in the magnonic band structures and SW propagation properties. However, in most of the cases, the properties of MCs, solely defined by their material and geometric parameters, remain invariant once the fabrication procedure is completed. The advanced technology requires on-demand, externally programmable MCs where the periodic modulation of magnetic properties can be dynamically switched "on" and "off" by external controllers such as magnetic (*5*) and electric fields (*6*). This opens up new possibilities for reprogrammable magnonics (*7*), which can bridge between cross-disciplinary fields such as photo-magnonics (*8*), mag-phonics (*9*), or spin-mechatronics (*10*). Most of the recent approaches in this regard are based on current-induced methods, which are critical for low-energy dissipation of magnetization in nanoscale magnetic elements because of the thermal stability issue. To overcome this obstacle, magneto-electric coupling (*11*) can become an efficient alternative approach to tailor the magnetic properties (e.g., magnetic anisotropy) using an electric field that has the overriding benefit of ultralow energy (power) consumption (*12*) because of the absence of ohmic dissipation, which is an inherent backlash in charge current–controlled magnonic devices (*13*).

The excitation and propagation of SWs along reconfigurable magnonic nanocircuits is the topic of intense interest in the field of magnonic applications. Consequently, SW nanochanneling through magnetic domain walls acting as reconfigurable SW nanochannels has been demonstrated (*14*). The SW modes propagating inside domain walls exhibit a well-defined wave vector along their propagation path, enabling data transport and processing using wave properties. This field has received further impetus with the experimental realization of SW propagation through antiferromagnetically coupled periodic arrays of 100-nm-wide stripe domains showing two different branches of SW, where the higher-frequency mode is accounted for the effective antiferromagnetic SW mode (*15*). Further experimental

[1]Department of Condensed Matter Physics and Material Sciences, S. N. Bose National Centre for Basic Sciences, Block JD, Sector III, Salt Lake, Kolkata 700 106, India. [2]Center for Emergent Matter Science, RIKEN, 2-1 Hirosawa, Wako 351-0198, Japan. [3]Research and Development Group, Hitachi Ltd., 1-280 Higashi-koigakubo, Kokubunji-shi, Tokyo 185-8601, Japan. [4]Institute for Solid State Physics, University of Tokyo, Kashiwa 277-8581, Japan.
*Corresponding author. Email: abarman@bose.res.in

work has shown injection of SW mode from a nanodisc to a domain wall nanochannel propagating at zero-bias magnetic field (*16*). While all these works have successfully used domain walls as magnonic nanochannel (MNC) for extracting important physics, the future device will require more ordered and well-defined nanochannels, properties of which can be ideally tuned continuously by external means. Recently, zero-field propagation of SWs through micrometer-wide waveguides defined by focused ion beam writing on a $Fe_{78}Ni_{22}$ layer by changing its structural phase and magnetic properties (*17*) has been demonstrated. Numerical simulations have shown that SWs can be confined within nanochannels generated by voltage-controlled magnetic anisotropy (VCMA) in an ultrathin ferromagnetic (FM) waveguide, where the width of the nanochannel is solely determined by the width of the electrode (*18*).

A plethora of theoretical and experimental investigations have demonstrated the electric field–induced control of magnetization in magnetic heterostructures including multiferroic materials (*19*), FM semiconductors (*20*), piezoelectric materials (*21*), or metallic FM/insulator (oxide) interfaces (*22*). Furthermore, parametric pumping of SWs by means of VCMA (*23*) and electric field control of SW power flow and caustics in thin magnetic films have also been demonstrated theoretically (*24*). FM/oxide interfaces have gained a substantial attention due to their superior control over magnetic parameters (e.g., anisotropy) at ambient condition as compared to other systems. The controlled manipulation of interfacial perpendicular magnetic anisotropy (iPMA) at the FM/oxide interfaces (*25*) has accelerated the possibilities of integrating reprogrammable devices with the future spin-based applications. Consequently, the investigation of VCMA or electric field–controlled magnetic anisotropy (ECMA) at the interfaces has received a great thrust in the recent times using both theoretical (*26*) and experimental approaches (*27*). Numerous strategies have been adopted for excitation, manipulation, channeling, and amplification of SWs, as well as the development of MCs and logic gates (*7*). Recently, SW tunneling, through a narrow magnetic barrier formed by local increase in magnetic anisotropy and the ensuing Hartman effect, has been demonstrated (*28*). On the other hand, the electrically controlled dynamic crystal has been presented in a magnetic insulator–based SW waveguide comprising a metallic meander structure situated close to its surface (*29*). Few studies have emphasized the operation of various functions (*30*) of magnonic devices (*31*) using electric field (voltage), in particular, through the modulation of PMA present at the interface of an FM metal and oxide heterostructure (*32*) complying with ultralow-power dissipation. These have triggered the quest for achieving a unusual genre of electric field–controlled magnonic devices such as reprogrammable multiplexer in recent times. To the best of our knowledge, experimental realization of reprogrammable electric field–controlled MNC (EFCMNC) has not been explored so far. In addition, interaction between the SWs propagating through the adjacent MNCs will be an interesting problem.

Here, we have taken this challenge to fabricate a dynamic EFCMNC array by using state-of-the-art nanofabrication and deposition tools. We have performed electric field–controlled SW dispersion measurements by Brillouin light scattering (BLS) technique (*33*) to demonstrate the emergence of magnonic band diagram of one-dimensional arrays of EFCMNC (1D-EFCMNC) consisting of an FM/oxide heterostructure. BLS has emerged as one of the most reliable tools to probe the dispersive nature of SW frequencies directly in the wave vector (k) domain. Unlike any other complementary method where external stimuli such as magnetic field, electric field, electrical current, or optical pumping (such as laser) are necessary to excite the SWs, BLS proves to be very effective as it can detect thermally excited magnons under ambient condition (i.e., room temperature). We have probed the magnonic band structure in an FM/oxide heterostructure consisting of 1D array of stripe-like electrodes serving as the top electrodes under the influence of an electric field (DC voltage) applied across the top (patterned) and bottom (unpatterned CoFeB film) electrodes. We have achieved a tunable band structure in the presence of a moderate electric field in the system, which vanishes after the electric field is removed. This remarkable observation is reaffirmed by measuring a similar magnetic heterostructure with unpatterned top electrodes, which unveils the absence of any magnonic band structure and BG with or without the electric field but only a gradual modulation of SW frequency with the applied voltage. This salient observation is well supported by the numerical calculations on the basis of plane wave method (PWM), which reproduced the SW dispersion behavior modified by the electric field. This confirms that an external electric field effectively tailors the iPMA present at the FM/oxide heterostructure, eventually generating such dynamic MNC whose magnonic band structure and magnonic BG can be switched on and off simply by the external electric field.

RESULTS

We have chosen the heterostructure substrate|Ta(10 nm)|$Co_{20}Fe_{60}B_{20}$ (1.6 nm)|MgO(2 nm)|Al_2O_3(10 nm) as the basis for the fabrication of the device under study. It is noteworthy that the magnetization state in an ultrathin CoFeB film strongly depends upon its thickness. Here, the magnetization direction tends to align along the out-of-plane (OOP) axis below a critical value of its thickness (~1.5 nm) (*34*). On the contrary, the magnetization tends to be aligned along the in-plane (IP) direction above the critical thickness. We have chosen the $Co_{20}Fe_{60}B_{20}$ (CoFeB) thickness to be 1.6 nm to ensure that its easy axis of magnetization lies in the sample plane. This is ensured from the anomalous Hall effect (AHE) measurement of the CoFeB/MgO heterostructure with an experimental scheme described in Fig. 1A. For this purpose, the CoFeB/MgO film was patterned into Hall bar structures with dimensions 80 μm by 400 μm. DC current (I_{DC}) of magnitude 0.5 mA was sent through the Hall bar from a current source, and the transverse Hall voltage (V_{AHE}) was measured by a nanovoltmeter while sweeping an OOP (i.e., along the x direction) magnetic field ($\mu_0 H$) from −500 mT to +500 mT as plotted in Fig. 1B. The absence of hysteresis loop and gradual switching of magnetization in Fig. 1B confirm an IP easy axis of magnetization of the sample. Furthermore, the IP magnetic hysteresis loop (shown in fig. S1A) was measured using vibrating sample magnetometry (VSM) from which the saturation magnetization ($\mu_0 M_s$) is calculated to be 1.5 T. In addition, the atomic force micrograph (AFM) for substrate|Ta(10 nm)|$Co_{20}Fe_{60}B_{20}$(1.6 nm)|MgO (2 nm)|Al_2O_3(10 nm) stack has been investigated to analyze the surface topography (shown in fig. S1B). Here, the average topographical roughness is calculated to be ~0.11 nm, which remains almost the same when measured at various regions of the same sample. Hence, we conclude that the topographical roughness is substantially small for the sample, which means that the average interfacial roughness, present in the heterostructure because of its small thickness, should also be very small.

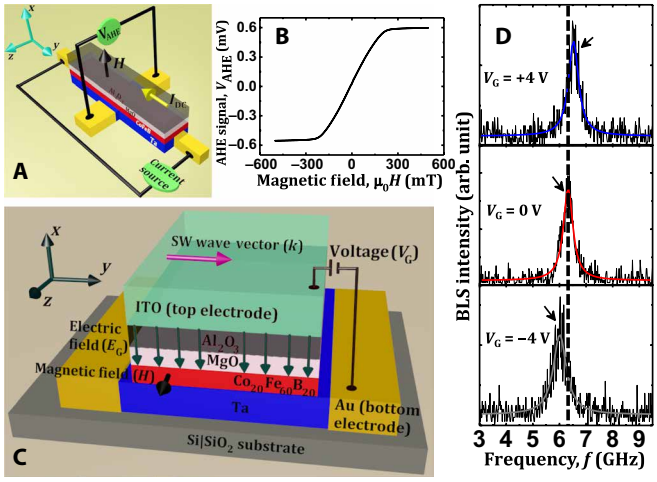

Fig. 1. Determination of magnetization easy axis and schematic of the sample along with the representative BLS spectra. (**A**) Schematic diagram of device structure and experimental setup for measuring AHE and (**B**) the corresponding measured AHE signal from the CoFeB/MgO heterostructure with CoFeB thickness (t_{CoFeB}) of 1.6 nm. (**C**) Schematic illustration of the CoFeB/MgO sample with a blanket ITO layer as the top electrode. (**D**) Stokes side of BLS spectra taken at IP transferred wave vector, $k = 2.05 \times 10^6$ rad m^{-1}, for applied gate voltage, $V_G = +4$, 0, and −4 V, respectively, in the presence of the bias magnetic field, $\mu_0 H = 200$ mT. The thick solid lines are theoretical fits with Lorentzian function, and the arrows describe the positions of the peak frequencies for $V_G = +4$, 0, and −4 V, respectively, while the dotted line clarifies the relative shift in the frequencies with respect to $V_G = 0$.

The principle behind the electric field modulation of iPMA in FM/oxide heterostructure

Generally, strong PMA can be observed at the interfaces between *3d* transition metal (or their alloys) FMs and heavy nonmagnetic (NM) metals, although iPMA cannot be modulated by an electric field in such systems because of the absence of insulating or dielectric layer at the interface. However, PMA can also be obtained at the FM/oxide interfaces. Among them, the CoFeB/MgO heterostructures (*34*) have drawn immense attention because of their application in magnetic tunnel junction (*35*). The reason for iPMA and VCMA at the CoFeB/MgO interface can be interpreted by the following approach. At the CoFeB/MgO interface, the OOP $3d_z^2$ orbitals of Fe strongly bond with OOP $2p_z$ orbitals of O, resulting in a significant charge transfer from $3d_z^2$ orbitals to $2p_z$ orbitals. Therefore, the number of electrons in OOP orbitals is reduced as compared to the number of electrons in IP orbitals, which introduces a considerable PMA through the spin-orbit coupling (SOC) of FM (*36*). When an electric field is applied across the FM/oxide interface, the number of electrons in the OOP 3*d* orbitals of Fe gets modified with respect to the IP orbitals as explained from first principles calculations (*37*). This affects the bonding strength between 3*d* and 2*p* orbitals, resulting in a substantial change of iPMA. Although electric field control of electronic occupation state is believed to be the main mechanism behind VCMA, several alternative theories are also found in the literature. One of the interesting theories claims the control of iPMA due to the coupling between magnetic dipoles and electric quadrupole of electronic orbital in FM, which is formed due to the inhomogeneous electric field at the FM/oxide interface (*38*). Another theory claims that the applied electric field at the FM/oxide interface modifies the Rashba SOC, which, in turn, modulates the iPMA (*39*). Recently, the piezoelectric property of the oxide (MgO) layer through magneto-elastic coupling is found to be responsible for the modulation of iPMA via development of tensile and compressive strain in the oxide layer (*40*). In reality, all the above mechanisms may be present and contribute simultaneously to the modulation of iPMA. Nevertheless, we believe that the presence of an oxide layer is essential for modulation of iPMA, where the relative change in the electronic occupation state in the 3*d* orbitals of FM plays a crucial role in achieving VCMA. In addition, because the penetration depth of the electric field in metal is only a few ångströms, the VCMA effect is only limited to ultrathin FM films. This justifies the choice of the ultrathin CoFeB film in our case.

Theoretical calculations reveal that the change in the number of electrons in 3*d* orbitals of FM scales linearly with the applied electric field (E_G) at the FM/oxide interface (*37*). Consequently, the change in the magnetic moment and iPMA should also be linearly proportional to the electric field (*22*), i.e.,

$$\Delta K_s = \beta E_G \tag{1}$$

Here, ΔK_s is the change in iPMA, while β is defined as the magnetoelectric or VCMA coefficient. The magnitude and sign of β depends upon several factors such as the composition of FM (*41*) or adjacent dielectric layer (*42*), underlayer material (i.e., the layer beneath the FM/oxide heterostructure) (*43*), substrate (*44*), and temperature (*45*).

Investigation of SW dispersion by probing thermally excited magnons

Figure 1C depicts the schematic illustration of the geometrical configuration adapted for the experimental investigation of SWs. Here, an unpatterned indium tin oxide (ITO) layer of thickness 120 nm has been deposited on top of the substrate|Ta(10 nm)|$Co_{20}Fe_{60}B_{20}$ (1.6 nm)|MgO(2 nm)|Al_2O_3(10 nm) heterostructure. This ITO layer serves as the top gate electrode to apply the electric field (E_G) or voltage (V_G) across the CoFeB/MgO interface. A positive gate voltage denotes that the top gate electrode has a positive potential with respect to the CoFeB film. All the measurements have been carried out in the Damon-Eshbach (DE) geometry, i.e., the (IP) SW wave vector (k) lies perpendicular to the magnetic field (H) applied in the plane of the sample. In Fig. 1D, we have presented typical BLS spectra measured at wave vector, $k = 2.05 \times 10^6$ rad m^{-1}, from a CoFeB/MgO heterostructure subjected to an IP magnetic field, $\mu_0 H$ = 200 mT for $V_G = +4$, 0, and −4 V. The BLS spectra are fitted using the Lorentzian function to extract the peak frequency value (f). It is evident from Fig. 1D that the SW frequency increases or decreases as a function of V_G depending upon the sign of V_G. To extract the magnetic parameter, especially the modulation in the iPMA field with V_G, we have measured the magnetic field ($\mu_0 H$) dependence of the SW frequency (f), which is represented in Fig. 2A for $V_G = +4$, 0, and −4 V. The values of iPMA fields have been extracted by fitting f versus $\mu_0 H$ data points with an analytical formula (*46*) as given below

$$f = \frac{\mu_0 \gamma}{2\pi}\left[\left(H + \frac{2A}{\mu_0 M_s}k^2\right)\left(H + \frac{2A}{\mu_0 M_s}k^2 + M_s - H_p(V_G)\right) + \frac{1}{4}M_s(M_s - H_p(V_G))\left(1 - e^{-2kt_{CoFeB}}\right)\right]^{\frac{1}{2}} \tag{2}$$

where γ, $H_p(V_G)$, M_s, and A represent the gyromagnetic ratio, iPMA field [which depends on the applied voltage (V_G) or electric field (E_G)], saturation magnetization, and exchange stiffness constant, respectively, and t_{CoFeB} denotes the thickness of the CoFeB layer, which is

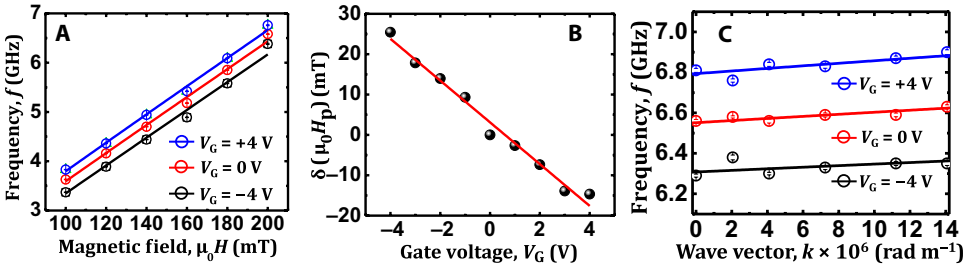

Fig. 2. Characterization of the CoFeB/MgO heterostructure with blanket ITO top electrode. (**A**) Variation of SW frequency as a function of bias magnetic field ($\mu_0 H$) obtained from the CoFeB/MgO heterostructure with a blanket ITO top electrode for three values of gate voltage, V_G = +4, 0, and −4 V. Symbols represent experimental data, while solid lines denote fitted curves using Eq. 2. (**B**) Variation of change in the iPMA field ($\mu_0 H_p$) as a function of V_G, where the solid line represents the linear fit. (**C**) Frequency (f) versus wave vector (k) dispersion curves for V_G = +4, 0, and −4 V. Symbols show the experimental data points, while solid lines describe the fits to the data points using Eq. 2. The error bars in experimental data are contained within the symbols.

1.6 nm in our case. Here, we have fixed the material parameters as $\gamma = 29.4$ GHz T^{-1}, $\mu_0 M_s = 1.5$ T, and $A = 28$ pJ m^{-1} (*18*) while setting $H_p(V_G)$ as a free parameter during the fitting of the field-dependent frequency data points. The extracted values of $\mu_0 H_p$ are found to be about 1.43, 1.45, and 1.47 T for V_G = +4, 0, and −4 V, respectively. As $\mu_0 M_s > \mu_0 H_p(V_G)$, the easy axis of magnetization always lies in the plane of the sample, which has already been confirmed from the AHE measurement.

In addition, we have extracted the anisotropy field [$\mu_0 H_p(V_G)$] using Eq. 2 for a number of the values of V_G (shown in fig. S1C). Now, to evaluate VCMA coefficient (β), i.e., the change of iPMA per unit gate voltage (V_G), the modulation of $\mu_0 H_p$, i.e., $\delta(\mu_0 H_p)$, as a function of V_G has been plotted in Fig. 2B. It is observed that the iPMA field varies linearly with V_G and the slope of this linear variation yields the value of β, which is calculated to be 5.17 mT V^{-1} in our CoFeB/MgO system. However, the conversion of β from mT V^{-1} to another unit, e.g., fJ V^{-1} m^{-1}, for 1.6-nm-thick CoFeB can be expressed by using Eq. 1 in the following way

$$\beta = \frac{d(\Delta K_s)}{d E_G} = \frac{1}{2} \cdot \left(\frac{\delta(\mu_0 H_p)}{\delta V_G} \right) \cdot \frac{\mu_0 M_s}{\mu_0} \cdot t_{CoFeB} \cdot t_{(MgO+Al_2O_3)} \quad (3)$$

The electric field (E) corresponding to V_G = 1 V is given by

$$E_G = \frac{1}{t_{(MgO+Al_2O_3)}} \text{V nm}^{-1} \quad (4)$$

while $t_{(MgO + Al_2O_3)}$ is the total thickness (12 nm) of the MgO and Al_2O_3 layer on top of CoFeB. Hence, the value of β becomes ~60 fJ V^{-1} m^{-1}. Figure 2C describes the SW dispersion (i.e., f versus k) relation measured at an applied IP field, $\mu_0 H$ = 200 mT for V_G = +4, 0, and −4 V, where k has been varied by changing the angle of incidence (θ) of the laser beam. It is noteworthy that SW frequency as a function of k acquired at all three different electric fields (E_G) has small dispersion. This is further confirmed by fitting the dispersion curves with the aid of Eq. 2 as represented in Fig. 2C, where the extracted values of $\mu_0 H_p(V_G)$ agree well with those calculated earlier from the magnetic field–dependent SW frequency curves in Fig. 2A.

Investigation of magnon dispersion in 1D-EFCMNC

We have investigated the SW dispersion in CoFeB/MgO heterostructure where the top ITO layer has been patterned in the form of a 1D array of stripes with width (w) of 220 nm and edge-to-edge separation (s) of 220 nm. This is designated as the 1D-EFCMNC as schematically depicted in Fig. 3A along with the experimental configuration. Here, these 1D stripes act as the top gate electrodes to apply the local and spatially periodic electric field (or voltage) across the CoFeB/MgO interface, while the bottom electrode remains unaltered as demonstrated in Fig. 3B. In Fig. 3 (C and D), we have presented the evolution of SWs with the wave vector (k) along the length of these nanochannels formed due to the modulation of iPMA by the applied voltage under the ITO electrodes. These representative BLS spectra have been acquired for wave vector values, $k = 2.05 \times 10^6$ rad m^{-1} and 7.1×10^6 rad m^{-1}, respectively, in the presence of V_G = −4 V (additional BLS spectra in this configuration for other wave vectors are presented in fig. S2). Here, an IP magnetic field, $\mu_0 H$ = 200 mT, has been set in the direction perpendicular to the stripe axis. This reveals a marked modulation in the BLS spectra where two clear SW modes are observed, which have been named as M1 and M2, respectively, according to their ascending order of frequency values. By carefully inspecting and analyzing the BLS spectra for all the wave vectors, we have found that a two-peak Lorentzian function correctly describes the BLS spectra (see figs. S2 and S3 for more details). We have investigated their full dispersion by varying the wave vector up to 14.2×10^6 rad m^{-1}, and Fig. 3E unveils the magnonic band structure of the 1D-EFCMNC at V_G = −4 V. The experimental data are shown by the symbols, while the calculated SW intensity obtained from PWM has been presented by the blue lines. The dispersion curves have been calculated using PWM by taking the modulation of iPMA field into account in the presence of an IP magnetic field, $\mu_0 H$ = 200 mT, applied to the sample plane similar to the experimental configuration. The experimental data points agree qualitatively well with the calculated results. In the experiment, the BLS spectra were characterized by the presence of two SW modes as depicted in Fig. 3 (C and D). As evident from Fig. 3E, both SW modes, i.e., M1 and M2, are dispersive modes, although their natures are different from each other. At $k \approx 7.1 \times 10^6$ rad m^{-1}, the modes experience a repulsion (anticrossing), causing M1 to change the sign of its dispersion and steepening of the dispersion of M2, opening a magnonic BG of ~0.37 GHz between these two modes.

As mentioned earlier, the iPMA has been modulated only in the regions underneath the periodically arranged top electrodes, which have been taken into account during PWM calculations. Hence, the magnetic anisotropy will be different in two regions as schematically described in Fig. 3B, i.e., (i) region 1 [$H_p(1)$], where the top electrodes are absent so that the effective magnetization [$M(1)$] will remain unaltered there, and (ii) region 2 [$H_p(2)$], which is underneath the top electrodes where the effective magnetization [$M(2)$] is dynamically

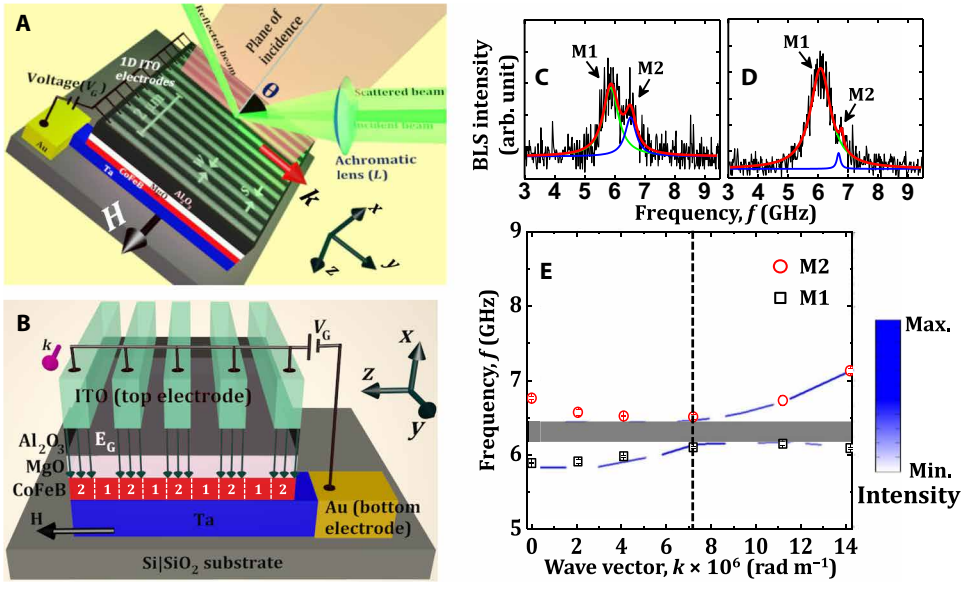

Fig. 3. Schematic of 1D-EFCMNC and its SW dispersion under the influence of applied voltage. (**A**) Schematic of the BLS measurement geometry used for the CoFeB/MgO heterostructure with 1D patterned ITO electrodes on top showing the incident (θ denotes the angle of incidence) and scattered light beams, the direction of the SW wave vector (*k*), and applied magnetic field H, with both vectors lying in the sample plane. (**B**) Periodic nature of electric field (E_G) applied at the CoFeB/MgO interface, giving rise to two periodic regions, where region 1: top electrodes are absent and region 2: underneath the top electrodes. Stokes side of the BLS spectra taken at $k = 2.05 \times 10^6$ rad m^{-1} (**C**) and $k = 7.1 \times 10^6$ rad m^{-1} (**D**), obtained for $V_G = -4$ V applied at $\mu_0 H = 200$ mT. The theoretical fits using Lorentzian functions are shown by thick solid lines, and the SW peaks (M1 and M2) are indicated by the arrows. (**E**) Magnonic band structure under the influence of $V_G = -4$ V applied at $\mu_0 H = 200$ mT. Symbols represent peak frequencies in the BLS spectra, while blue lines denote SW intensities as calculated by PWM (the corresponding color map is given at the right side). The dashed vertical line indicates the position of anticrossing, and the corresponding magnonic BG is shown by the shaded region. The error bars in experimental data are contained within the symbols.

tailored in the presence of an electric field or voltage (V_G) as $H_p(2)$ depends on both magnitude and sign of V_G. In our case,

$$H_p(1) < H_p(2), \text{for } V_G < 0 \quad (5)$$

$$H_p(1) > H_p(2), \text{for } V_G > 0 \quad (6)$$

To get a closer insight into the SW propagation character in the presence of the 1D-EFCMNC, we have calculated the SW mode profiles by plotting the spatial distribution of the *x* component of dynamic magnetization, i.e., the modulus of the SW amplitude, of the relevant experimentally observed SW modes.

The spatial maps of these two SW modes (M1 and M2) are depicted in Fig. 4 for $k = 2.05 \times 10^6$ rad m^{-1} and 7.1×10^6 rad m^{-1}, (i.e., far below and near the anticrossing region), respectively, calculated for $V_G = -4$ V. Here, the dotted lines divide two different regions (1: regions without top electrodes and 2: regions with top electrodes, respectively) as discussed earlier. As represented in Fig. 4, both M1 and M2 are DE-like modes, i.e., extended along the *y* direction perpendicular to the direction of *H* (which is along the *z* direction as described in Fig. 3A). However, we have observed a stark difference in the characteristics of M1 and M2 as the SW intensity of M1 is completely localized in region 1, while SW intensity of M2 is primarily concentrated in region 2. As depicted in Fig. 4A for $k = 2.05 \times 10^6$ rad m^{-1}, M1 has a confined nature along the *z* direction in the backward volume (BV) geometry with quantization number, $n = 1$ (i.e., the nodal planes being perpendicular to *H*) in region 1, while M2 shows a BV-like nature in region 2, again with $n = 1$. Both the modes have

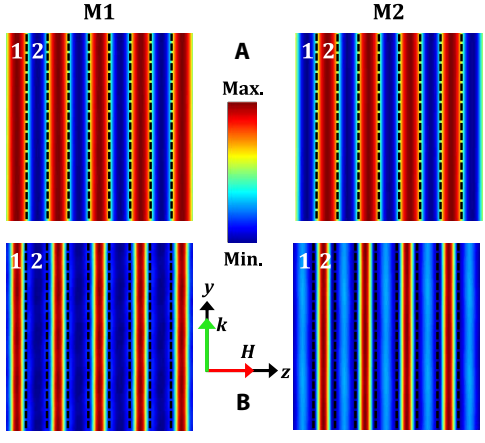

Fig. 4. SW nanochanneling in 1D-EFCMNC in the presence of an applied voltage. Spatial profiles of the SW modes for $k = 2.05 \times 10^6$ rad m^{-1} (**A**) and $k = 7.1 \times 10^6$ rad m^{-1} (**B**) under the application of $V_G = -4$ V at $\mu_0 H = 200$ mT. The color map and the geometry of *H* are shown at the center of the figure. Here, region 1 denotes the area without the top electrode, while region 2 represents the area beneath the top electrode.

similar profile covering nearly the whole width of the 1D stripe–like nanochannels defined by the presence or absence of the electrodes. As we move to the higher wave vector, i.e., $k = 7.1 \times 10^6$ rad m^{-1} as described in Fig. 4B, the nature of the mode profiles of M1 and M2 remain identical. However, spatial extents of both the modes get

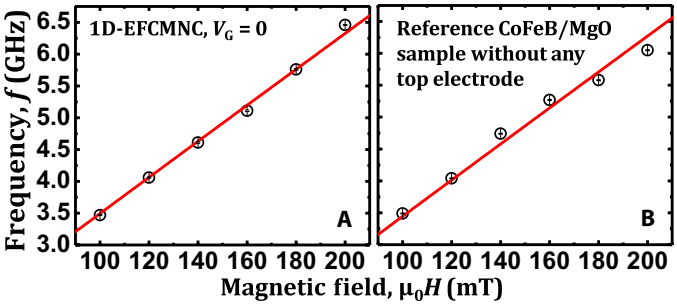

Fig. 5. Reconfigurability of 1D-EFCMNC. Variation of SW frequency as a function of bias magnetic field ($\mu_0 H$) at $k = 2.05 \times 10^6$ rad m^{-1} obtained from (**A**) the CoFeB/MgO heterostructure with 1D patterned ITO electrodes without gate voltage, i.e., $V_G = 0$, and (**B**) the reference CoFeB/MgO sample without any top electrode. The solid lines represent the fits with Eq. 2. The error bars in experimental data are contained within the symbols.

sharply reduced as the modes become more confined near the center of the nanochannels. This is most likely due to the mode repulsion causing the anticrossing between the modes M1 and M2.

The SW dispersion diagram after reversing the polarity of the electric field (i.e., for $V_G = +4$ V) is shown in fig. S4. Here, again, two SW modes have been observed and both of them have dispersive behavior with the variation in k with a BG of ~0.26 GHz due to SW mode anticrossing. The calculated SW intensities at $k = 0$ and 7.1×10^6 rad m^{-1} also confirm the variation in the frequency spacing between the SW modes with wave vector. The spatial profiles of the SW modes M1 and M2 in this voltage configuration have also been calculated at $k = 2.05 \times 10^6$ rad m^{-1} and 7.1×10^6 rad m^{-1}, respectively, which are shown in fig. S5. At $k = 2.05 \times 10^6$ rad m^{-1}, the spatial profiles of M1 and M2 are completely opposite to those observed at $V_G = -4$ V. In this case, M1 is localized in region 2, while M2 is localized in region 1. At $k = 7.1 \times 10^6$ rad m^{-1}, the spatial nature of M1 and M2 remains unaltered, although their spatial extents again get slightly reduced along the z direction and confined near the center of the nanochannels. Therefore, such dynamic control of SW nanochanneling induced by VCMA has a fascinating property of bipolar tunability depending upon the sign of bias voltage.

To investigate the reconfigurable property of this 1D-EFCMNC system, we probed its SW dynamics without any gate voltage. The bias field–dependent SW frequency for the 1D-EFCMNC is presented in Fig. 5A at $k = 2.05 \times 10^6$ rad m^{-1} by setting $V_G = 0$. The result reveals a monotonic variation of SW frequency with H. This variation is identical to that obtained for a CoFeB/MgO heterostructure with unpatterned top electrode acquired at $V_G = 0$ as shown in Fig. 2A. Incidentally, both of these bias field–dependent SW frequencies resemble to that recorded from a reference CoFeB/MgO film without any top electrode as shown in Fig. 5B. The experimental SW dispersion relations obtained for both the above cases (fitted using Eq. 2) at $\mu_0 H = 200$ mT are presented in fig. S6. This demonstrates that the voltage applied to the patterned 1D array of stripe-like electrodes on the CoFeB/MgO heterostructure can efficiently toggle the 1D-EFCMNC between its active and passive state. The requirement of a small voltage for the onset of the active state ensures that it can be reset perfectly to its pristine thin film–like state by removing that voltage. This development may pave the way to next generation reprogrammable magnonic devices controllable by electric field with minimum ohmic dissipation as well as for studying strong magnon-magnon coupling in MNCs.

DISCUSSION

We have developed a voltage controlled on-demand MNC array on the basis of the principle of VCMA in CoFeB/MgO heterostructure. We have performed a combined experimental and theoretical investigation of the reconfigurable magnonic band structure in this dynamic MNC by varying the applied gate voltage. The SW dispersion in this new class of MNC has been measured by probing thermal magnons using BLS spectroscopy. First, we attained a monotonic enhancement or decrement in the SW frequency by varying the strength and polarity of the electric field applied to the CoFeB/MgO heterostructure with an unpatterned top gate electrode due to VCMA. Further analysis corroborates the linear dependence of iPMA with the applied electric field. We then probed the SW dynamics of the CoFeB/MgO heterostructure by patterning 1D array of ITO electrodes on the top of it. A magnonic band structure consisting of two SW frequency modes along with a BG appear under the application of a modest electric field. The spatial profiles of the SW modes unravel an intriguing bipolar tunability of such dynamic MNC. This SW dispersion reverts to its original state for the unpatterned electrode with the disappearance of the BG as soon as the electric field is withdrawn. This demonstrates the achievement of a reprogrammable and dynamic magnonic band structure by an electric field across the CoFeB/MgO interface applied through patterned 1D array of stripe-like electrodes. This unlocks a gateway to develop a new genre of MNCs invoked by an energy-efficient stimulus, i.e., electric field, which may play a key role in devising spin-based magnonic nanocircuits with ultralow-power consumption.

MATERIALS AND METHODS

Sample preparation

The samples were prepared by multistep fabrication method. First, the multilayered heterostructure was deposited on Si(001)|SiO_2(700 nm) substrate by radio frequency sputtering at room temperature at a base pressure of about 1×10^{-8} torr. The structure of multilayer stack is Si|SiO_2|Ta(10)|$Co_{20}Fe_{60}B_{20}$(1.6)|MgO(2)|Al_2O_3(10), where the numbers in parentheses represent the nominal thicknesses (in nanometers) of the corresponding layers. The sputter-deposited film stack was then annealed at 280°C in vacuum under a perpendicular magnetic field of 600 mT for 1 hour. Because PMA present in the heterostructure is interfacial (i.e., at the CoFeB/MgO interface) in nature, the thickness of CoFeB is chosen to be 1.6 nm to enhance the magneto-electric effect while keeping the easy axis of magnetization in the plane of the sample at the same time. In the second step, square blanket area of lateral dimensions 70 μm by 70 μm was prepared from the annealed multilayer stacks by using maskless ultraviolet (UV) photolithography followed by Ar^+ ion milling down to SiO_2. In the third step, alignment markers for electron beam lithography and metal gate (bottom) electrodes were prepared by maskless UV photolithography followed by deposition of the Ti(5)|Au(100) layer by electron beam evaporation. In the fourth step, Al_2O_3 with 100 nm thickness was deposited everywhere except on top of the square area and the metal electrodes. In the fifth step, electron beam lithography was used to prepare the 1D grid–like pattern on the top

of the sample, which was followed by deposition of a 120-nm-thick ITO layer (top gate electrode) by DC sputtering technique. Here, each stripe-like top gate electrode has a width of 220 nm with an edge to edge separation of 220 nm (i.e., pitch = 440 nm). It is noteworthy that ITO was chosen as the top electrode due to its transparent nature, which is essential for the optical (BLS) measurement through the electrodes to acquire thermally excited magnons from the CoFeB/MgO heterostructure. In the last step, all the contacts for application of DC gate voltage were made by maskless photolithography and deposition of the Ti(5)|Au(200) layer by electron beam evaporation. Two reference samples, one with the CoFeB/MgO heterostructure without any top electrode and another with an unpatterned 120-nm-thick ITO layer as the top electrode, were also prepared using a similar procedure.

Measurement technique

BLS experiments were performed in the conventional backscattering configuration for the measurement of dispersion characteristics of thermal magnons in the sample. This technique relies on the inelastic light scattering process arising from the interaction between incident photons and magnons. Monochromatic laser beam (wavelength, λ = 532 nm, power ≈ 65 mW) from a solid-state laser was focused on the surface of the sample. The diameter of the focused laser spot is about 40 μm, which is smaller than the lateral dimensions of the sample (60 μm by 60 μm). The laser beam was carefully placed on the sample, which was further confirmed by using an imaging setup with white light illumination and charge-coupled device camera. The laser beam is inelastically scattered from the magnons, and the magnitude of the IP transferred wave vector (k) depends on the incidence angle (θ) of light according to the relation

$$k = \frac{4\pi}{\lambda}\sin\theta \tag{7}$$

Cross-polarizations between the incident and the scattered beams are adopted during the experiment to minimize the phonon contribution to the scattered light. Subsequently, the frequencies of the scattered light were analyzed using a Sandercock-type six-pass (3 + 3) tandem Fabry-Pérot interferometer (JRS Scientific Instruments). There, a frequency shift is observed along with the laser frequency taking into account the energy and momentum conservation. The BLS spectra were recorded after counting photons for several hours to achieve well-defined magnon spectra in all the cases. A free spectral range (FSR) of 30 GHz and a 2^{10} multichannel analyzer were used during the BLS measurement. The digital frequency resolution is determined by estimating FSR/2^{10} (≈30 MHz) for the Stokes (or the anti-Stokes) peaks of the BLS spectra, while the instrument response function is about 0.18 GHz as obtained from the Rayleigh peak (fig. S2A). Here, the direction of the wave vector (k) was kept parallel to the axes of the 1D stripe–like top electrodes, i.e., along the y direction as described in Fig. 3A, by making the stripe axes parallel to the light scattering plane throughout the experiment [off-axis propagation (*47*)]. The BLS spectra were recorded for up to $k = 14.2 \times 10^6$ rad m^{-1}. The SW dispersion was performed at an IP magnetic field, $\mu_0 H = 200$ mT, applied to the sample. The electric field is applied by a DC voltage source (Keithley 2450 source meter) between the top and bottom electrodes of the sample without the presence of any leakage current through the heterostructure (this was confirmed simultaneously while applying the electric field throughout the experiment).

Theoretical calculation

We have numerically calculated the spectrum of magnonic excitations of the dynamic 1D-EFCMNC using PWM, which is a robust tool because of its conceptual simplicity and its applicability to periodically patterned network with varying shape of the scattering centers. We solve the Landau-Lifshitz (LL) equation for the magnetization [$\boldsymbol{M} = M(\boldsymbol{r}, t)$] under the influence of an effective magnetic field, H_{eff}, which can be primarily expressed as a sum of different field contributions as

$$H_{\text{eff}} = H + H_{\text{ex}} + H_{\text{d}} + H_{\text{ani}} \tag{8}$$

where H, H_{ex}, H_{d}, and H_{ani} represent the applied static magnetic field, exchange field, magnetostatic or demagnetizing field, and anisotropy field, respectively. The experimental outcomes justify the neglecting of the damping and nonreciprocity in the model. $M(\boldsymbol{r}, t)$ is written as

$$M(\boldsymbol{r}, t) = M_{\text{s}}(\boldsymbol{r}) + m(\boldsymbol{r}, t) \tag{9}$$

Here, $M_{\text{s}}(\boldsymbol{r})$ and $m(\boldsymbol{r}, t)$ describe the components of $M(\boldsymbol{r}, t)$ parallel (constant in time) and perpendicular to H while considering linear approximation under the condition

$$|M_{\text{s}}(\boldsymbol{r})| \gg |m(\boldsymbol{r}, t)| \tag{10}$$

For a magnetically inhomogeneous medium (such as a 1D-EFCMNC in our case), the spatial inhomogeneity of the material parameters, e.g., spontaneous magnetization and exchange constant as well as the magnetostatic field, has been considered during the calculation so that

$$H_{\text{d}}(\boldsymbol{r}, t) = H_{\text{d}}(\boldsymbol{r}) + h_{\text{d}}(\boldsymbol{r}, t) \tag{11}$$

where $H_{\text{d}}(\boldsymbol{r})$ and $h_{\text{d}}(\boldsymbol{r}, t)$ are static and dynamic components of $H_{\text{d}}(\boldsymbol{r}, t)$ fulfilling the Maxwell equations, while

$$h_{\text{d}}(\boldsymbol{r}, t) = h_{\text{d}}(\boldsymbol{r})\, e^{i2\pi ft} \tag{12}$$

$$m(\boldsymbol{r}, t) = m(\boldsymbol{r})\, e^{i2\pi ft} \tag{13}$$

In addition, H_{ex} can be expressed as

$$H_{\text{ex}}(\boldsymbol{r}, t) = (\vec{\nabla} . \lambda_{\text{ex}}^2(\boldsymbol{r})\, \vec{\nabla})\, m(\boldsymbol{r}, t) \tag{14}$$

where $\lambda_{\text{ex}}(\boldsymbol{r})$ denotes the exchange length, which is related to exchange stiffness constant [$\mathbf{A} = A(\boldsymbol{r})$] as

$$\lambda_{\text{ex}}^2(\boldsymbol{r}) = \frac{2A(\boldsymbol{r})}{\mu_0 M_{\text{s}}^2} \tag{15}$$

Subsequently, the Fourier transformation has been carried out to map all the periodic functions (in space and time) including the static and dynamic parts of the magnetic fields and magnetization components to the reciprocal space using Bloch's theorem (*48*). Considering the lattice periodicity, a (in our case, $w = s = 220$ nm, so that $a = w + s = 440$ nm), $m(\boldsymbol{r})$ can be expressed as

$$m(\boldsymbol{r}) = \Sigma_G m_k(G)\, e^{i(\boldsymbol{k}+\boldsymbol{G}).\boldsymbol{r}} \tag{16}$$

where **G** represents the reciprocal lattice vector of the considered MNC so that

$$G = (G_y, G_z) = \frac{2\pi}{a}(n_y, n_z) \quad (17)$$

with n_y and n_z being integers. In the studied case, the wave vector k lies along the axes of the stripe-like 1D electrodes, i.e., $k = k_y$ as shown in Fig. 3A, so that we can now write

$$G = (G_y, G_z) = \frac{2\pi}{a}(0, n_z) \quad (18)$$

Consequently, Eq. 16 will represent a plane wave (not a Bloch wave) for SW propagating along the y direction with its amplitude modulated in the z direction (i.e., the amplitude will not be modulated by the lattice along the y direction). Being a periodic function of position in the 1D-EFCMNC, the saturation magnetization (M_s) and $(\lambda_{ex})^2$ can be mapped onto the reciprocal space using the Fourier transformation formulas as

$$M_s(\boldsymbol{r}) = \Sigma_G M_s(\boldsymbol{G})\, e^{i\boldsymbol{G}.\boldsymbol{r}} \quad (19)$$

$$\lambda_{ex}^2(\boldsymbol{r}) = \Sigma_G \lambda_{ex}^2(\boldsymbol{G})\, e^{i\boldsymbol{G}.\boldsymbol{r}} \quad (20)$$

where the Fourier coefficients are determined analytically. It is noteworthy that the 1D-EFCMNC in our case has been dynamically created by applying the electric field through the 1D patterned top electrodes to periodically modulate the PMA at the CoFeB/MgO interface. Hence, the anisotropy field, i.e., H_{ani}, in Eq. 8 originates from the PMA at the CoFeB/MgO interface such that

$$H_{ani} = H_{ani}(V_G) \quad (21)$$

In other words, this system behaves as MNCs, which are composed of two exchange-coupled magnetic media having contrasting magnetic anisotropy, where the anisotropy in the area (region 2 in our case as shown in Fig. 3B) under top electrodes either increases or decreases periodically (i.e., H_{ani} also has periodic nature in the reciprocal space similar to M_s) depending upon the sign of the applied voltage (V_G). Hence, in our case for the 1D-EFCMNC, the expressions for the static magnetization (M_s) can be calculated (*49*) in the reciprocal space as

$$M_s(G) = \frac{w}{a} M_{s,\text{Region1}} + M_{s,\text{Region2}}\left(1 - \frac{w}{a}\right) \text{ for } G = 0 \quad (22)$$

$$= \frac{2}{Ga}(M_{s,\text{Region1}} - M_{s,\text{Region2}}) \sin\left(G\frac{w}{2}\right) \text{for } G \neq 0 \quad (23)$$

Here, $M_{s,\text{Region1}}$ and $M_{s,\text{Region2}}$ represent the M_s values at regions 1 (remains unaltered with V_G) and 2 (controllable by V_G, i.e., by the electric field), respectively. Thus, the PWM transforms the LL equation into a set of algebraic equations, which leads to an eigenvalue problem. To find the eigenvalues (the frequencies of SWs) and eigenvectors (amplitude of the dynamic component of **M**), the Fourier series has to be limited to the finite number of elements. The eigenvalue problem is then solved with standard numerical routines. A satisfactory convergence of the numerical solutions of the eigenvalue problem has been obtained by taking 450 plane waves in our case.

SUPPLEMENTARY MATERIALS

Supplementary material for this article is available at http://advances.sciencemag.org/cgi/content/full/6/40/eaba5457/DC1

REFERENCES AND NOTES

1. J. Shi, P. Zhang, D. Xiao, Q. Niu, Proper definition of spin current in spin-orbit coupled systems. *Phys. Rev. Lett.* **96**, 076604 (2006).
2. D. Grundler, Reconfigurable magnonics heats up. *Nat. Phys.* **11**, 438–441 (2015).
3. V. V. Kruglyak, S. O. Demokritov, D. Grundler, Magnonics. *J. Phys. D Appl. Phys.* **43**, 260301 (2010).
4. A. V. Chumak, V. I. Vasyuchka, A. A. Serga, B. Hillebrands, Magnon spintronics. *Nat. Phys.* **11**, 453–461 (2015).
5. C. Banerjee, S. Choudhury, J. Sinha, A. Barman, Pseudo-one-dimensional magnonic crystals for high-frequency nanoscale devices. *Phys. Rev. Appl.* **8**, 014036 (2017).
6. Q. Wang, A. V. Chumak, L. Jin, H. Zhang, B. Hillebrands, Z. Zhong, Voltage-controlled nanoscale reconfigurable magnonic crystal. *Phys. Rev. B* **95**, 134433 (2017).
7. M. Krawczyk, D. Grundler, Review and prospects of magnonic crystals and devices with reprogrammable band structure. *J. Phys. Condens. Matter* **26**, 123202 (2014).
8. J. W. Kłos, M. Krawczyk, Y. S. Dadoenkova, N. N. Dadoenkova, I. L. Lyubchanskii, Photonic-magnonic crystals: Multifunctional periodic structures for magnonic and photonic applications. *J. Appl. Phys.* **115**, 174311 (2014).
9. P. Graczyk, M. Krawczyk, Coupled-mode theory for the interaction between acoustic waves and spin waves in magnonic-phononic crystals: Propagating magnetoelastic waves. *Phys. Rev. B* **96**, 024407 (2017).
10. M. Matsuo, E. Saitoh, S. Maekawa, Spin-mechatronics. *J. Phys. Soc. Jpn.* **86**, 011011 (2017).
11. F. Matsukura, Y. Tokura, H. Ohno, Control of magnetism by electric fields. *Nat. Nanotechnol.* **10**, 209–220 (2015).
12. T. Nozaki, Y. Shiota, S. Miwa, S. Murakami, F. Bonell, S. Ishibashi, H. Kubota, K. Yakushiji, T. Saruya, A. Fukushima, S. Yuasa, T. Shinjo, Y. Suzuki, Electric-field-induced ferromagnetic resonance excitation in an ultrathin ferromagnetic metal layer. *Nat. Phys.* **8**, 491–496 (2012).
13. S. I. Kiselev, J. C. Sankey, I. N. Krivorotov, N. C. Emley, R. J. Schoelkopf, R. A. Buhrman, D. C. Ralph, Microwave oscillations of a nanomagnet driven by a spin-polarized current. *Nature* **425**, 380–383 (2003).
14. K. Wagner, A. Kákay, K. Schultheiss, A. Henschke, T. Sebastian, H. Schultheiss, Magnetic domain walls as reconfigurable spin-wave nanochannels. *Nat. Nanotechnol.* **11**, 432–436 (2016).
15. C. Liu, S. Wu, J. Zhang, J. Chen, J. Ding, J. Ma, Y. Zhang, Y. Sun, S. Tu, H. Wang, P. Liu, C. Li, Y. Jiang, P. Gao, D. Yu, J. Xiao, R. Duine, M. Wu, C.-W. Nan, J. Zhang, H. Yu, Current-controlled propagation of spin waves in antiparallel, coupled domains. *Nat. Nanotechnol.* **14**, 691–697 (2019).
16. L.-J. Chang, J. Chen, D. Qu, L.-Z. Tsai, Y.-F. Liu, M.-Y. Kao, J.-Z. Liang, T.-S. Wu, T.-M. Chuang, H. Yu, S.-F. Lee, Spin wave injection and propagation in a magnetic nanochannel from a vortex core. *Nano Lett.* **20**, 3140–3146 (2020).
17. L. Flajšman, K. Wagner, M. Vaňatka, J. Gloss, V. Křižáková, M. Schmid, H. Schultheiss, M. Urbánek, Zero-field propagation of spin waves in waveguides prepared by focused ion beam direct writing. *Phys. Rev. B* **101**, 014436 (2020).
18. B. Rana, Y. Otani, Voltage-controlled reconfigurable spin-wave nanochannels and logic devices. *Phys. Rev. Appl.* **9**, 014033 (2018).
19. P. Rovillain, R. de Sousa, Y. Gallais, A. Sacuto, M. A. Méasson, D. Colson, A. Forget, M. Bibes, A. Barthélémy, M. Cazayous, Electric-field control of spin waves at room temperature in multiferroic $BiFeO_3$. *Nat. Mater.* **9**, 975–979 (2010).
20. H. Ohno, D. Chiba, F. Matsukura, T. Omiya, E. Abe, T. Dietl, Y. Ohno, K. Ohtani, Electric-field control of ferromagnetism. *Nature* **408**, 944–946 (2000).
21. M. Xu, J. Puebla, F. Auvray, B. Rana, K. Kondou, Y. Otani, Inverse Edelstein effect induced by magnon-phonon coupling. *Phys. Rev. B* **97**, 180301(R) (2018).
22. C.-G. Duan, J. P. Velev, R. F. Sabirianov, Z. Zhu, J. Chu, S. S. Jaswal, E. Y. Tsymbal, Surface magnetoelectric effect in ferromagnetic metal films. *Phys. Rev. Lett.* **101**, 137201 (2008).
23. R. Verba, M. Carpentieri, G. Finocchio, V. Tiberkevich, A. Slavin, Excitation of spin waves in an in-plane-magnetized ferromagnetic nanowire using voltage-controlled magnetic anisotropy. *Phys. Rev. Appl.* **7**, 064023 (2017).
24. V. N. Krivoruchko, A. S. Savchenko, V. V. Kruglyak, Electric-field control of spin-wave power flow and caustics in thin magnetic films. *Phys. Rev. B* **98**, 024427 (2018).
25. T. Maruyama, Y. Shiota, T. Nozaki, K. Ohta, N. Toda, M. Mizuguchi, A. A. Tulapurkar, T. Shinjo, M. Shiraishi, S. Mizukami, Y. Ando, Y. Suzuki, Large voltage-induced magnetic anisotropy change in a few atomic layers of iron. *Nat. Nanotechnol.* **4**, 158–161 (2009).
26. T. Kawabe, K. Yoshikawa, M. Tsujikawa, T. Tsukahara, K. Nawaoka, Y. Kotani, K. Toyoki, M. Goto, M. Suzuki, T. Nakamura, M. Shirai, Y. Suzuki, S. Miwa, Electric-field-induced changes of magnetic moments and magnetocrystalline anisotropy in ultrathin cobalt films. *Phys. Rev. B* **96**, 220412(R) (2017).
27. M. Weisheit, S. Fähler, A. Marty, Y. Souche, C. Poinsignon, D. Givord, Electric field-induced modification of magnetism in thin-film ferromagnets. *Science* **315**, 349–351 (2007).
28. J. W. Kłos, Y. S. Dadoenkova, J. Rychły, N. N. Dadoenkova, I. L. Lyubchanskii, J. Barnaś, Hartman effect for spin waves in exchange regime. *Sci. Rep.* **8**, 17944 (2018).

29. A. D. Karenowska, J. F. Gregg, V. S. Tiberkevich, A. N. Slavin, A. V. Chumak, A. A. Serga, B. Hillebrands, Oscillatory energy exchange between waves coupled by a dynamic artificial crystal. *Phys. Rev. Lett.* **108**, 015505 (2012).
30. U. Bauer, S. Emori, G. S. D. Beach, Voltage-controlled domain wall traps in ferromagnetic nanowires. *Nat. Nanotechnol.* **8**, 411–416 (2013).
31. W.-G. Wang, M. Li, S. Hageman, C. L. Chien, Electric-field-assisted switching in magnetic tunnel junctions. *Nat. Mater.* **11**, 64–68 (2011).
32. B. Rana, Y. Otani, Towards magnonic devices based on voltage-controlled magnetic anisotropy. *Commun. Phys.* **2**, 90 (2019).
33. S. O. Demokritov, B. Hillebrands, A. N. Slavin, Brillouin light scattering studies of confined spin waves: Linear and nonlinear confinement. *Phys. Rep.* **348**, 441–489 (2001).
34. S. Ikeda, K. Miura, H. Yamamoto, K. Mizunuma, H. D. Gan, M. Endo, S. Kanai, J. Hayakawa, F. Matsukura, H. Ohno, A perpendicular-anisotropy CoFeB–MgO magnetic tunnel junction. *Nat. Mater.* **9**, 721–724 (2010).
35. H. Ohno, Toward functional spintronics. *Science* **291**, 840–841 (2001).
36. H. X. Yang, M. Chshiev, B. Dieny, J. H. Lee, A. Manchon, K. H. Shin, First-principles investigation of the very large perpendicular magnetic anisotropy at Fe|MgO and Co|MgO interfaces. *Phys. Rev. B* **84**, 054401 (2011).
37. M. Tsujikawa, T. Oda, Finite electric field effects in the large perpendicular magnetic anisotropy surface Pt / Fe / Pt(001): A first-principles study. *Phys. Rev. Lett.* **102**, 247203 (2009).
38. S. Miwa, M. Suzuki, M. Tsujikawa, K. Matsuda, T. Nozaki, K. Tanaka, T. Tsukahara, K. Nawaoka, M. Goto, Y. Kotani, T. Ohkubo, F. Bonell, E. Tamura, K. Hono, T. Nakamura, M. Shirai, S. Yuasa, Y. Suzuki, Voltage controlled interfacial magnetism through platinum orbits. *Nat. Commun.* **8**, 15848 (2017).
39. S. E. Barnes, J. Ieda, S. Maekawa, Rashba spin-orbit anisotropy and the electric field control of magnetism. *Sci. Rep.* **4**, 4105 (2014).
40. V. B. Naik, H. Meng, J. X. Xiao, R. S. Liu, A. Kumar, K. Y. Zeng, P. Luo, S. Yap, Effect of electric-field on the perpendicular magnetic anisotropy and strain properties in CoFeB/MgO magnetic tunnel junctions. *Appl. Phys. Lett.* **105**, 052403 (2014).
41. A. Okada, S. Kanai, M. Yamanouchi, S. Ikeda, F. Matsukura, H. Ohno, Electric-field effects on magnetic anisotropy and damping constant in Ta/CoFeB/MgO investigated by ferromagnetic resonance. *Appl. Phys. Lett.* **105**, 052415 (2014).
42. D. D. Lam, F. Bonell, S. Miwa, Y. Shiota, K. Yakushiji, H. Kubota, T. Nozaki, A. Fukushima, S. Yuasa, Y. Suzuki, MgO overlayer thickness dependence of perpendicular magnetic anisotropy in CoFeB thin films. *J. Korean Phys. Soc.* **62**, 1461–1464 (2013).
43. Y. Shiota, F. Bonell, S. Miwa, N. Mizuochi, T. Shinjo, Y. Suzuki, Opposite signs of voltage-induced perpendicular magnetic anisotropy change in CoFeB|MgO junctions with different underlayers. *Appl. Phys. Lett.* **103**, 082410 (2013).
44. Y. Hayashi, Y. Hibino, F. Matsukura, K. Miwa, S. Ono, T. Hirai, T. Koyama, H. Ohno, D. Chiba, Electric-field effect on magnetic anisotropy in Pt/Co/Pd/MgO structures deposited on GaAs and Si substrates. *Appl. Phys. Express* **11**, 013003 (2017).
45. Y. Hibino, T. Koyama, A. Obinata, T. Hirai, S. Ota, K. Miwa, S. Ono, F. Matsukura, H. Ohno, D. Chiba, Peculiar temperature dependence of electric-field effect on magnetic anisotropy in Co/Pd/MgO system. *Appl. Phys. Lett.* **109**, 082403 (2016).
46. B. A. Kalinikos, A. N. Slavin, Theory of dipole-exchange spin wave spectrum for ferromagnetic films with mixed exchange boundary conditions. *J. Phys. C* **19**, 7013–7033 (1986).
47. J. D. Joannopoulos, R. D. Meade, J. N. Winn, S. G. Johnson, P. U. Press, *Photonic Crystals: Molding the Flow of Light* (Princeton Univ. Press, 1995).
48. M. Krawczyk, H. Puszkarski, Plane-wave theory of three-dimensional magnonic crystals. *Phys. Rev. B* **77**, 054437 (2008).
49. M. L. Sokolovskyy, M. Krawczyk, The magnetostatic modes in planar one-dimensional magnonic crystals with nanoscale sizes. *J. Nanopart. Res.* **13**, 6085–6091 (2011).

Acknowledgments: We thank S. Majumder for technical assistance. **Funding:** A.B. gratefully acknowledges financial support from S. N. Bose National Centre for Basic Sciences (SNBNCBS), Kolkata under grant number SNB/AB/18-19/211. Y.O. and B.R. gratefully acknowledge financial support from Grant-in-Aid for Scientific Research on Innovative Area, "Nano Spin Conversion Science" (grant number 26103002). B.R. acknowledges RIKEN Incentive Research Project grant number FY2019. S.C. and A.K.M. acknowledge SNBNCBS, and A.K.C. acknowledges DST for INSPIRE fellowship (number IF150922). **Author contributions:** A.B., B.R., and Y.O. planned and supervised the project. K.M. and H.T. prepared the thin-film heterostructure, and S.C. and B.R. fabricated the patterned devices. S.C. and A.K.C. did the measurements and analyses in consultation with A.B. and B.R. A.K.M. and S.C. performed the theoretical calculations in discussion with A.B. S.C. and A.B. wrote the manuscript in consultation with other coauthors. **Competing interests:** The authors declare that they have no competing interest. **Data and materials availability:** All data needed to evaluate the conclusions in the paper are present in the paper and/or the Supplementary Materials. Additional data related to this paper may be requested from the authors.

Submitted 12 December 2019
Accepted 13 August 2020
Published 2 October 2020
10.1126/sciadv.aba5457

Citation: S. Choudhury, A. K. Chaurasiya, A. K. Mondal, B. Rana, K. Miura, H. Takahashi, Y. Otani, A. Barman, Voltage controlled on-demand magnonic nanochannels. *Sci. Adv.* **6**, eaba5457 (2020).

Science Advances

Voltage controlled on-demand magnonic nanochannels

Samiran Choudhury, Avinash Kumar Chaurasiya, Amrit Kumar Mondal, Bivas Rana, Katsuya Miura, Hiromasa Takahashi, YoshiChika Otani and Anjan Barman

Sci Adv **6** (40), eaba5457.
DOI: 10.1126/sciadv.aba5457